

Mechanical stress dependence of the Fermi level pinning on an oxidized silicon surface

H. Li¹, L. Martinelli¹, F. Cadiz¹, A. Bendounan², S. Arscott³, F. Sirotti¹, and A.C.H. Rowe^{1*}

¹*Physique de la Matière Condensée, Ecole Polytechnique,
CNRS, Université Paris-Saclay, 91128 Palaiseau, France*

²*Synchrotron SOLEIL, L'Orme des Merisiers Saint-Aubin, 91192 Gif-sur-Yvette, France and*

³*Institut d'Electronique, de Microélectronique et de Nanotechnologie (IEMN),
Université de Lille, CNRS, Avenue Poincaré, Cité Scientifique, 59652 Villeneuve d'Ascq, France*

A combination of micro-Raman spectroscopy and micro-XPS (X-ray photo-electron spectroscopy) mapping on statically deflected p-type silicon cantilevers is used to study the mechanical stress dependence of the Fermi level pinning at an oxidized silicon (001) surface. With uniaxial compressive and tensile stress applied parallel to the $\langle 110 \rangle$ crystal direction, the observations are relevant to the electronic properties of strain-silicon nano-devices with large surface-to-volume ratios such as nanowires and nanomembranes. The surface Fermi level pinning is found to be even in applied stress, a fact that may be related to the symmetry of the Pb_0 silicon/oxide interface defects. For stresses up to 160 MPa, an increase in the pinning energy of 0.16 meV/MPa is observed for compressive stress, while for tensile stress it increases by 0.11 meV/MPa. Using the bulk, valence band deformation potentials the reduction in surface band bending in compression (0.09 meV/MPa) and in tension (0.13 meV/MPa) can be estimated.

As semiconductor electronic devices continue to shrink in size, surface-to-volume ratios increase and the electronic properties of the surface become more important to the overall device characteristics. In particular, the energy at which the surface Fermi level is pinned due to interface defects can significantly modify both the electronic [1] and optical [2] properties of semiconductor nano-objects. In some cases this has been identified as a means to produce new device functionalities [3], while in other cases it demands changes to device design rules [4]. In parallel with reductions in device size, mechanical stress is also a key ingredient of the so-called semiconductor road map, designed to help evaluate technical innovations in the micro-electronics industry [5].

In strained silicon technologies, stress is used to improve the *bulk* electronic properties of CMOS devices [6] but there is some evidence from electrical transport measurements, including studies of gate leakage currents in MOS devices [7] and data retention times in flash memory devices [8], that it also modifies the electronic properties of deep defect states at the silicon/oxide interface. Recently, the stress-dependence of surface Fermi level pinning by these states has been implicitly invoked to explain unusual piezo-resistive behavior in silicon nano-objects [9–11] and giant piezo-impedance observed during space-charge-limited-current transport in silicon-on-insulator (SOI) [12]. Interpretation of these transport phenomena is often difficult because they yield only indirect access to a physically important quantity, the stress-induced change surface Fermi level pinning due to changes in the activation energy of interface defects [13].

Here, the mechanical stress-induced change in the surface Fermi level pinning at a natively-oxidized silicon (001) surface is studied spectroscopically using surface

science tools, in particular X-ray photo-electron spectroscopy (XPS) of the Si 2p core levels [14, 15]. Using the known values of the bulk valence band deformation potentials [16, 17] it is then possible to obtain a spectroscopic estimation of the stress-dependence of the surface band bending.

Experiments are performed on macroscopic silicon cantilevers fabricated using standard lithographic methods. The boron doped ($\rho < 0.01 \Omega\text{cm}$) device layer is 5 μm thick, the buried oxide layer is 1 μm thick and the handle is $d = 400 \mu\text{m}$ thick. Once processed (see Supplementary Material), the wafer is diced with a diamond saw into cantilevers $l = 11 \text{ mm}$ long and $b = 3 \text{ mm}$ with the long axis parallel to the $\langle 110 \rangle$ crystal direction (see Fig. 1(a)). The cantilevers are protected during this procedure with a 1 μm thick photo-resist layer and were subsequently stored with the photo-resist in place for two months. Two weeks prior to the experiments reported here, the photo-resist was removed and the surfaces rinsed in acetone, iso-propyl alcohol and de-ionized water. No further surface treatment was made prior to XPS experiments, a conscience choice made in order to study surfaces more relevant to nano-scale electronic devices than the usual reconstructed surfaces used in XPS studies.

The cantilevers are loaded into sample mounts (seen in Fig. 1(a)) with their fixed ends firmly clamped to the mount while the free ends can be deflected upwards or downwards using an actuator screw as shown in Figs. 1(b) and (c). This classic cantilevered beam with a free-end point load [18] results in a uni-axial compressive (tensile) stress parallel to the $\langle 110 \rangle$ crystal direction at the top surface for an upwards (downwards) deflection of the free end. Its magnitude is maximum at the fixed end and falls linearly to zero at the free end [18]. The neutral bending axis is approximately at the vertical center of the handle so that the uni-axial stress obtained in this way is approximately constant across the device layer thickness. The (maximum) stress at the fixed end is ob-

* alistair.rowe@polytechnique.edu

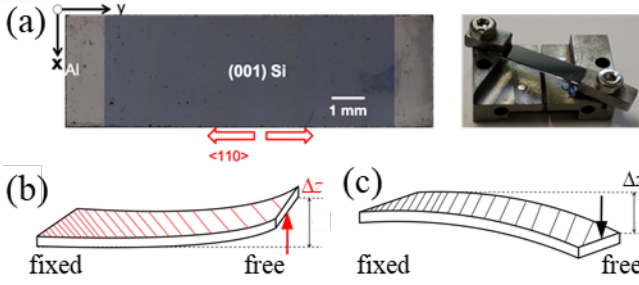


FIG. 1. (a) p-type silicon cantilevers with ohmic contacts visible at each end that make contact with the earthed sample holder shown right. Using a mechanical screw to apply a force as shown in (b) and (c), the free end of the cantilever is deflected by Δz . (b) An upwards deflection yields a uniaxial, compressive stress parallel to the $\langle 110 \rangle$ crystal direction on the top surface, with a maximum at the fixed end. (c) A downwards deflection yields an equivalent tensile stress.

tained using the formula $X_{\max} = 3Ed\Delta z/2l^2$ where $E = 170$ GPa is Youngs modulus of silicon along the $\langle 110 \rangle$ crystal direction [19]. Using the cantilever dimensions given above, for a typical deflection of $\Delta z = 0.2$ mm, a maximum stress magnitude of approximately 170 MPa at the fixed end is expected. This is experimentally verified on statically deflected cantilevers by measuring the sign and magnitude of the stress via the shift in the LO phonon Raman peak [20] as a function of position along the length and width of the cantilever.

Using the usual convention for mechanical stress (compressive stress is negative, tensile stress is positive) maps of the statically applied stress on two cantilevers, one in compression, one in tension, are obtained (see Fig. 2). Not only do the maps indicate a quasi-linear increase in the stress from the free to the fixed end, but the order of magnitude is in agreement with that estimated from textbook formulae [18]. Without any further adjustment of the actuator screw, a spatial map of the kinetic energy, E_k , of electrons photo-emitted from the Si 2p core levels is made. Since the stress is a function of position, a combination of kinetic energy and Raman maps can be used to determine the shift in the Si 2p core level position with mechanical stress for a single value of the cantilever deflection, Δz .

XPS experiments were performed on the ultra-high vacuum (UHV) experimental station of the TEMPO beamline at the Soleil synchrotron using a Scienta SES 2002 electron energy analyzer operated in the swept and fixed modes with a $E_{\text{ph}} = 200$ eV photo-excitation and a 100 eV pass energy. Under these conditions intense Si 2p core level peaks from silicon atoms within a 0.12 nm mean free path [21, 22] of the silicon/silicon oxide interface can be obtained. This extreme interface sensitivity permits a measurement of the stress-dependence of the surface Fermi level pinning energy according to the graphical arguments given in Fig. 3(a). The photon energy, E_{ph} and the analyzer work function, Φ , are independent of stress whereas stress modifies the core level binding en-

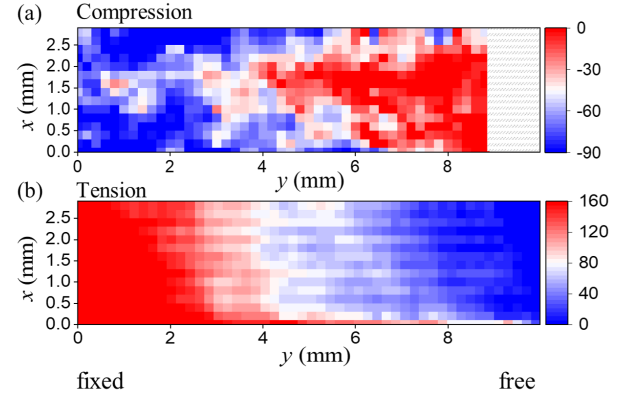


FIG. 2. Maps of the uniaxial mechanical stress applied parallel to the y -direction obtained using micro-Raman spectroscopy for a cantilever whose top surface is under compression (a) and tension (b). Color bars correspond to the measured stress in MPa.

ergy, E_b , the valence (E_{VB}) and conduction band (E_{CB}) edges [16], and the activation energy of interface defects, E_a [13] at which the surface Fermi level is pinned. The stress-dependence of the photo-emitted electron kinetic energy, E_k is then equal (but opposite) to E_a . As indicated by the black ($X = 0$) and red ($X > 0$) in Fig. 3(a), knowledge of the stress-dependence of the E_{VB} can then be used to translate this into the stress-dependence of the band bending itself.

Fig. 3(b) shows example Si 2p core level spectra plotted as a function of E_k for three different tensile stresses, 0 MPa (red), 80 MPa (blue) and 160 MPa (black). The shift due to the applied stress is clear from the raw data shown (inset). With an SES analyzer energy resolution of about 50 meV, and using the usual Voigt function fitting procedure [23, 24], the relative positions of intense Si 2p core level peaks can be determined to within approximately 1 meV (see the Supplementary Material). In the fitting procedure each state is represented by a doublet with a spin-orbit splitting of 0.6 eV, and an intensity ratio 1:2 between 1/2 and 3/2 spin-orbit split states. The intensity, area, kinetic energy shift, and Gaussian broadening of the Voigt functions for the spectrum shown in Fig. 3(b) are summarized in Table I.

This procedure is carried out for each pixel in the E_k map, obtained by scanning the cantilever in 100 μm steps under the soft X-ray beam which is focused to a Gaussian spot of half width ≈ 100 μm . In order to correlate the relative core level peak positions to the applied stress an oxide-thickness related correction must first be applied to the data. As seen in the Supplementary Material the oxide thickness is found to be systematically thicker near the edges of the cantilevers, a fact attributed to the 2-month storage time mentioned above. Unfortunately, oxide thickness influences the Si 2p core level binding energies [25] so that in order to extract a stress-dependence of E_a , the spatial variation of the oxide thickness must be accounted for. This is achieved by extracting (for

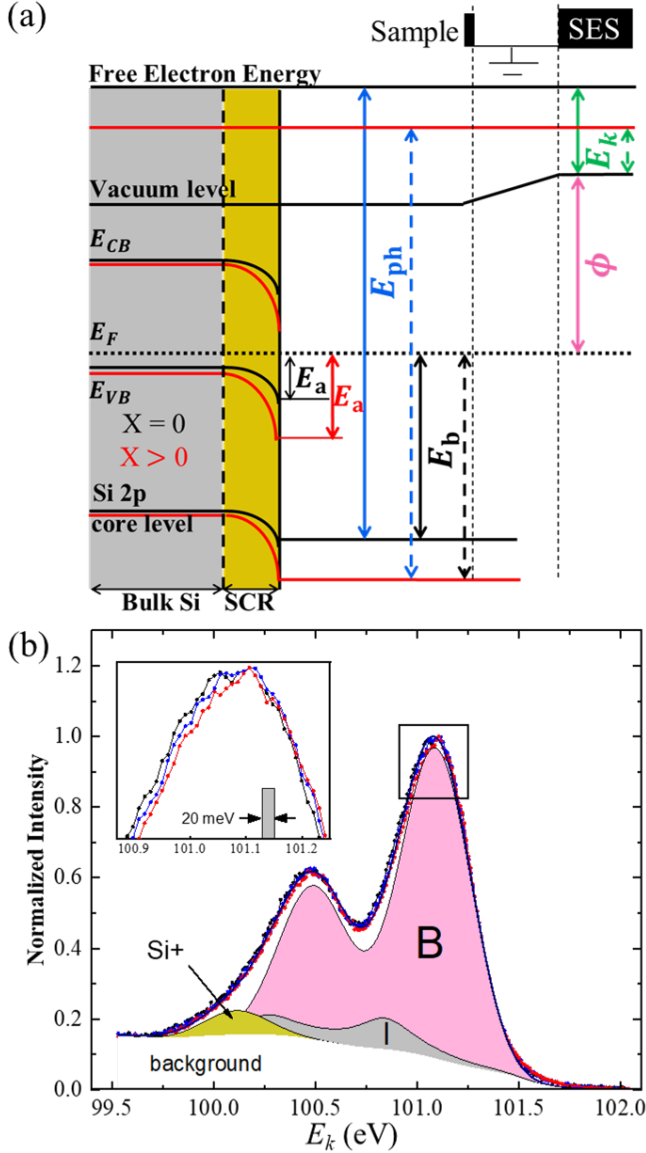


FIG. 3. (a) Energy level diagram for the surface of p-type silicon showing the electronic structure in the bulk and in the space charge region (SCR) with (red) and without (black) stress. (b) An example of a normalized Si 2p core level XPS spectrum from atoms within 0.12 nm of the silicon/oxide interface for three values of stress, 0 MPa (red), 80 MPa (black) and 160 MPa (blue). Each core level is fitted using Voigt doublets with the parameters shown in Table I.

each value of the coordinate x) only pixels whose oxide thickness is the same along the y -direction, at least to within an arbitrarily imposed 2 % variation around some mean value. The pixel color in Fig. 4(a) then represents the binding energy relative to the average value obtained in the rectangle at the free (i.e. zero stress) end of the cantilever. The remaining pixels, shown in gray, are not longer used in the following analysis.

In Figs. 4(a) and (b), the stress-induced E_a shifts, calculated from the kinetic energy of photo-electrons

TABLE I. The fitting parameters used in Fig. 3(b).

Core level	Label	Intensity $\times 10^5$	Rel. E_k shift (eV)	Width (eV)
Si 2p	B	22.1	0	0.4
Si 2p 2 nd plane	I	1.2	-0.25	0.35
Si+	Si+	2.08	-0.99	0.38

Figure 4(a) shows a map of the surface Fermi level pinning energy, E_a , under compressive stress. The x-axis is y (mm) from 0 to 8, and the y-axis is x (mm) from 0 to 2. A color bar indicates E_a shift (meV) from 0 to 16. A gray rectangle is at $y=0$ and $x=0$. A red rectangle is at $y=0$ and $x=1$. A green rectangle is at $y=6$ and $x=1$. A yellow rectangle is at $y=8$ and $x=1$.

Figure 4(b) shows a map of the surface Fermi level pinning energy, E_a , under tensile stress. The x-axis is y (mm) from 0 to 8, and the y-axis is x (mm) from 0 to 2. A color bar indicates E_a shift (meV) from 0 to 25. A gray rectangle is at $y=0$ and $x=0$. A red rectangle is at $y=0$ and $x=1$. A green rectangle is at $y=6$ and $x=1$. A yellow rectangle is at $y=8$ and $x=1$.

Figure 4(c) shows histogram plots of the relative E_a of the pixels shown in the colored rectangles of (a). The x-axis is E_a shift (meV) and the y-axis is Count. The red histogram has a mean of 14.6 ± 1.1 meV. The green histogram has a mean of 6.5 ± 0.7 meV. The yellow histogram has a mean of 1.5 ± 0.4 meV.

FIG. 4. Maps of the surface Fermi level pinning energy, E_a , relative to that obtained at the free end of the cantilever as a function of beam position under (a) compressive stress and (b) tensile stress. The active (colored) pixels shown in maps are selected because they have the same oxide thickness. (c) The histogram plots of the relative E_a of the pixels shown in the colored rectangles of (a). The mean and standard error values of these data, represented as a black line and a gray box respectively, are combined with the micro-Raman spectroscopy data to obtain E_a as a function of applied stress.

emitted from the Si 2p 3/2 core level according to the schematic in Fig. 3(a), are seen to be large and positive around the fixed end ($y = 0$ mm) of the cantilever for both compressive and tensile stresses, the first suggestion that E_a exhibits an even response in applied stress. These two maps are separated into areas containing approximately the same number of pixels (15), denoted by the gray rectangles. The pixels in the red, green and yellow rectangles on the compressively stressed surface are selected to demonstrate how the data is subsequently plotted in Fig. 5(a). The data histograms from these three rectangles are shown, color coded, in Fig. 4(c). The stress-induced shift in the center-of-mass of these histograms is clearly visible, moving from lower E_a shifts in the yellow rectangle (free end) to higher E_a shifts in the red rectangle (fixed end). In each rectangle the mean and standard error of E_a shifts are calculated and marked in Fig. 4(c) with a black line and gray box respectively. From the fixed to the free end they are 14.6 ± 1.1 meV, 6.5 ± 0.7 meV and 1.5 ± 0.4 meV respectively. These values, which are relatively robust to changes in the rectangle sizes (i.e. the number of points chosen in each rectangle) establish the mean E_a shift as a function of the mean y -position of the pixels in each rectangle. By performing a similar procedure using the same pixels in the Raman maps of Fig. 2, it is then possible to obtain a plot, shown in Fig. 5(a), of the stress-induced E_a shift

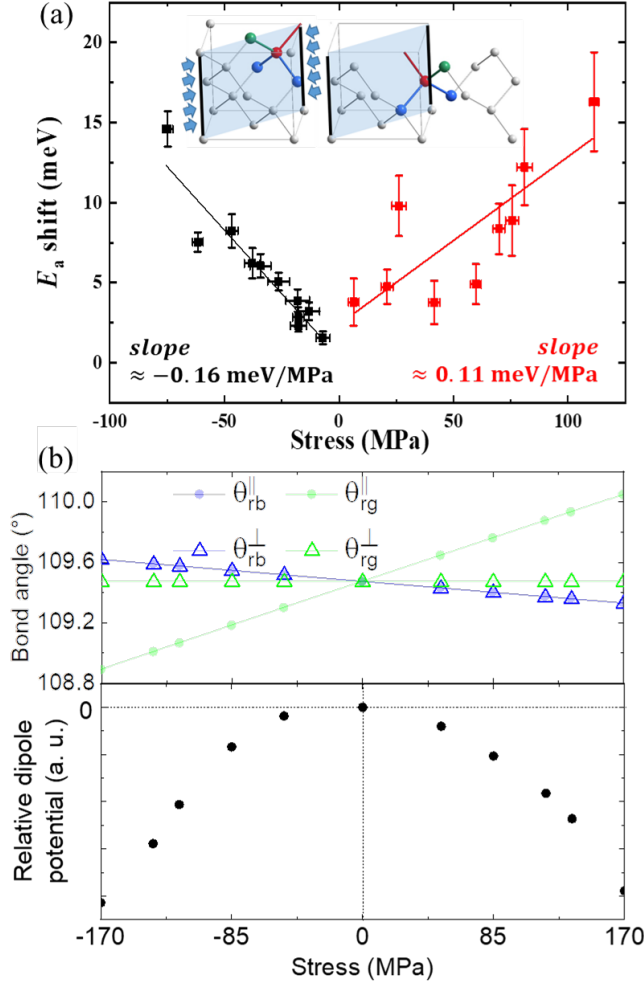


FIG. 5. (a) The E_a shift exhibits an even response in stress. The inset shows the two possible orientations of the Pb_0 defect at the (001) surface. Stress is applied in the $\langle 110 \rangle$ direction, and the case of compression is indicated by the blue arrows. The blue $\langle 1\bar{1}0 \rangle$ plane serves as a guide to the eye. (b) The stress induced changes in bond angles versus strain, the blue curves correspond to the changes in bond angle between the red dangling bond and the blue back bonds; the green curves correspond to that between the red dangling bond and the green bond. (c) The estimated Coulomb potential energy of an electron in the red dangling bond with respect to stress.

versus the applied stress.

The result of this procedure, shown in Fig. 5(a), makes the even response in stress explicitly clear. In compression E_a increases by 0.16 meV/MPa while for tensile stresses it increases by 0.11 meV/MPa. These stress-induced shifts can be converted into a stress-dependence of the surface band bending i.e. the difference between the valence band edge in the bulk, and the valence band edge at the silicon/oxide interface shown in Fig. 3(a). In order to estimate this it is necessary to account for the stress-induced shifts in the bulk valence bands [16] which are known from piezoresistance measurements on p-type silicon [17]. Both heavy (HH) and light hole (LH) bands

shift to higher energies under compressive stress, with deformation potentials of approximately -3.75 eV and -12.5 eV respectively. Note that the negative sign accounts for the fact that by convention compressive stresses are negative. Using these values, the Youngs modulus of silicon, and the known applied stress levels, the surface band bending reduces by 0.09 meV/MPa in compression, and by 0.13 meV/MPa in tension.

The even symmetry of the E_a shift is unusual compared to stress-induced variations in bulk electronic levels which are odd in stress, but it is consistent with interface leakage currents measurements [7, 8]. The exact origin of this even symmetry is not clear, but the symmetry of the intrinsic Pb_0 Si/SiO₂ was previously speculated to be responsible [7, 8]. This interpretation is comforted by the fact that stress-induced shifts in E_a of Si/SiO₂ interface traps obtained by indirect transport measurements on MOS capacitors are of similar magnitude [13] to the shifts obtained here.

To explore this idea further, Fig. 5(b) shows the two possible Pb_0 interface defect structures on a (001) silicon surface. In the left structure, referred to as the parallel geometry, the red dangling bond points in the $\langle 111 \rangle$ crystal direction and therefore has a spatial component parallel to the $\langle 110 \rangle$ crystal direction along which stress is applied. In the right panel of Fig. 5(b), referred to as the perpendicular geometry, the red, dangling bond points in the $\langle 1\bar{1}1 \rangle$ crystal direction and therefore has a spatial component perpendicular to the $\langle 110 \rangle$ crystal direction. In both cases the stress can be visualized as a force applied uniformly along the thick, black edges of the unit cell parallel to the light blue plane. The arrows in the left panel of Fig. 5(b) represent the applied force that yields in a uni-axial tensile stress. In the following, a simple relative estimation of the Coulomb potential at the end of the dangling bond due to the electronic charge present in the back bonds (shown in blue and green) will be made as a function of the applied stress. The motivation for this [8] is the notion that this energy will determine E_a for Pb_0 interface traps.

Using the compliance tensor for silicon [19], the effect of applied stress on the bond angles, and hence on the relative changes in distance between the ends of the bonds can be estimated. This can then be used to estimate the stress-induced changes to the total Coulomb potential at the dangling bond. The calculated changes in the back bond angles are shown in Fig. 5(c). For a tensile stress the bond angle between the red dangling bond and green back bond in the parallel geometry, θ_{rg}^{\parallel} , increases (see filled, green circles in Fig. 5(c)), while for the perpendicular geometry, θ_{rg}^{\perp} slightly decreases due to Poissons effect (see filled, green triangles in Fig. 5(c)). A compressive stress results in the opposite behavior. The bond angle between the red dangling bond and the blue back bonds in the parallel geometry, θ_{rb}^{\parallel} , decreases under tensile stress due to Poissons effect (see filled, blue circles in Fig. 5(c)), while in the perpendicular geometry, θ_{rb}^{\perp} , decreases (see filled, blue triangles in Fig. 5(c)). Again,

the opposite is true for a compressive stress. A simple geometric calculation, assuming constant bond lengths, then yields a relative estimate of the Coulomb potential as a function of applied stress, and this is found to be even in stress, despite the fact that the bond angles themselves are odd in stress. This is possible because the stress-induced changes to $\theta_{\text{rg}}^{\parallel}$ are partially compensated by opposite changes in $\theta_{\text{rb}}^{\parallel}$ and $\theta_{\text{rb}}^{\perp}$. While this is not proof that the symmetry of the Pb_0 centers is the sole origin of the even response in the stress-dependence of E_a , it is a proof of principle that two odd angular contributions can result in an overall even response.

Although the XPS measurements of the stress-dependence of E_a presented here provide important design parameters for nano-scale, strained-silicon devices, further progress towards a better physical understand-

ing of the even stress-dependence of E_a will require a more detailed calculation of the stress-dependence of the electronic trap eigenvalues, for example using ab initio methods [26].

I. SUPPLEMENTARY MATERIALS

The Supplementary Material contains full details of the sample fabrication procedure, along with details of the oxide thickness variation across the cantilever surface.

ACKNOWLEDGMENTS

This work was partially financed by the French Agence Nationale de la Recherche, contract ANR-17-CE24-0005. The authors thank F. Rochet for useful discussions.

-
- [1] M. G. Kibria, S. Zhao, F. A. Chowdhury, Q. Wang, H. P. T. Nguyen, M. L. Trudeau, H. Guo, and Z. Mi, *Nature Communications* **5**, 3825 (2014).
 - [2] O. Demichel, M. Heiss, J. Bleuse, H. Mariette, and A. Fontcuberta i Morral, *Applied Physics Letters* **97**, 201907 (2010).
 - [3] Q. Wan, Q. H. Li, Y. J. Chen, T.-H. Wang, X. L. He, J. P. Li, and C. L. Lin, *Applied Physics Letters* **84**, 3654 (2004).
 - [4] N. G. Shankar and Z. W. Zhong, *Microelectronic engineering* **77**, 337 (2005).
 - [5] *The international technology roadmap for semiconductors 2.0, metrology chapter* (2014), URL <https://eps.ieee.org/images/files/Roadmap/ITRSMetro12015.pdf>.
 - [6] J. Hoyt, H. Nayfeh, S. Eguchi, I. Aberg, G. Xia, T. Drake, E. Fitzgerald, and D. Antoniadis, in *Electron Devices Meeting, 2002. IEDM'02. International* (IEEE, 2002), pp. 23–26.
 - [7] Y. Choi, T. Nishida, and S. Thompson, *Appl. Phys. Lett.* **92**, 173507 (2008).
 - [8] A. Toda, S. Fujieda, K. Kanamori, J. Suzuki, K. Kuroyanagi, N. Kodama, Y. Den, and O. Nishizaka, in *Reliability Physics Symposium, 2005. Proceedings. 43rd Annual. 2005 IEEE International* (2005), pp. 250–256.
 - [9] A. C. H. Rowe, *Nature Nanotech.* **3**, 311 (2008).
 - [10] Y. Yang and X. Li, *Nanotechnology* **22**, 015501 (2010).
 - [11] Y. Yang and X. Li, *IEEE Electron Device Letters* **32**, 411 (2011).
 - [12] H. Li, C. T. K. Lew, B. Johnson, J. C. McCallum, S. Arscott, and A. C. H. Rowe, arXiv:1801.09494v4 [cond-mat.mes-hall] (2018).
 - [13] A. Hamada and E. Takeda, *IEEE Elec. Dev. Lett.* **15**, 31 (1994).
 - [14] J. A. Yarmoff, D. K. Shuh, T. D. Durbin, C. W. Lo, D. A. Lapiano-Smith, F. R. McFeely, and F. J. Himpsel, *Journal of Vacuum Science & Technology A* **10**, 2303 (1992).
 - [15] D. Pierucci, J. Gallet, F. Bournel, F. Sirotti, M. Silly, H. Tissot, A. Naitabdi, and F. Rochet, *The Journal of Physical Chemistry C* **120**, 21631 (2016).
 - [16] J. Hensel and G. Feher, *Physical Review* **129**, 1041 (1963).
 - [17] J. S. Milne, I. Favorskiy, A. C. H. Rowe, S. Arscott, and C. Renner, *Physical Review Letters* **108**, 256801 (2012).
 - [18] T. Hicks, *Civil engineering formulas* (McGraw-Hill, 2002).
 - [19] J. Wortman and R. Evans, *Journal of Applied Physics* **36**, 153 (1965).
 - [20] I. De Wolf, *Semiconductor Science and Technology* **11**, 139 (1996).
 - [21] M. Hochella Jr and A. H. Carim, *Surface Science* **197**, L260 (1988).
 - [22] M. Morita, T. Ohmi, E. Hasegawa, M. Kawakami, and M. Ohwada, *Journal of Applied Physics* **68**, 1272 (1990).
 - [23] E. Landemark, C. Karlsson, Y. Chao, and R. Uhrberg, *Physical Review Letters* **69**, 1588 (1992).
 - [24] J. Gallet, M. Silly, M. El Kazzi, F. Bournel, F. Sirotti, and F. Rochet, *Scientific Reports* **17**, 14257 (2017).
 - [25] T. Eickhoff, V. Medicherla, and W. Drube, *Journal of electron spectroscopy and related phenomena* **137**, 85 (2004).
 - [26] J. Godet, F. Giustino, and A. Pasquarello, *Phys. Rev. Lett.* **99**, 126102 (2007).